

## Research paper

## Astro Pi sensor onboard the International Space Station as magnetic field surveyor

Adrian Blagau<sup>a,\*</sup>, Andrei Ersen<sup>b</sup>, Corina Dobrescu<sup>b</sup>, Octav Marghitu<sup>a</sup><sup>a</sup> Institute for Space Sciences, 409 Atomistilor Street, Magurele, Ilfov, 077125, Romania<sup>b</sup> Tudor Vianu National High School of Computer Science, 10 Arh. Ion Mincu Street, Bucharest, 011358, Romania

## ARTICLE INFO

## Keywords:

Astro Pi Challenge  
International Space Station  
Magnetic field observations  
ISS magnetic field proper

## ABSTRACT

The Astro Pi sensor onboard the International Space Station (ISS) provides, among others, magnetic field information with a resolution of some 300 nT. Starting from an experiment proposed to ESA by a high school team and subsequent ISS observations under the Astro Pi Challenge Mission Space Lab, the paper demonstrates the good agreement of these observations with a geomagnetic field model and explores the potential for using the Astro Pi as magnetic field surveyor. Since ISS is not tuned for magnetic field observations and is not magnetically clean, a difficulty along this line is to extract from the observed data the magnetic field contributed by ISS, accomplished here by an optimization procedure. For now, the accuracy of the results is limited mainly by the Astro Pi sensor performance, whose resolution compares rather well to the third harmonic terms of the magnetic field model, and by the lack of attitude information. In principle, this can be improved by a better sensor (or sensors) of known orientation and by more sophisticated data processing algorithms. Magnetic field data from satellites that are not targeted to magnetic field observations, including commercial ones, are currently used for various monitoring and modeling purposes. By appropriate developments, ISS could provide as well useful magnetic field data, observed in particular at very low altitudes, rarely reached by satellites.

## 1. Introduction

The Astro Pi Challenge Mission Space Lab is an European Space Agency (ESA) Education project/competition organized yearly in collaboration with the Raspberry Pi Foundation [1]. Under this framework, teams of people aged 19 or younger, supervised by a teacher, are offered the opportunity to design and program an experiment to be run on Raspberry Pi computers onboard the International Space Station (ISS). In the first phase of the challenge, the teams have to come up with their own idea of an experiment and submit a proposal. In the second stage, teams whose experiments are accepted receive an Astro Pi kit that mimics the Raspberry Pi computers onboard, to write and test their data acquisition software. After a final check by ESA, the selected experiments are carried on, by running the respective acquisition codes over 3 h windows on the ISS Raspberry Pi computers. In the last phase, the teams analyze the data received from ISS and prepared their final reports. For the 2020/21 edition, 232 teams completed their tasks, out of 428 teams that initially submitted a proposal.

The present paper has been triggered by the proposal submitted by team Narwhals, from the Tudor Vianu National High School of Computer Science in Bucharest, supervised by Prof. Corina Dobrescu,

with high school student Andrei Ersen assuming the leading role. After submitting the proposal and while preparing for the phase of data analysis and interpretation, the team approached researchers from the Institute for Space Sciences in Bucharest (ISSB) to help in overcoming the problem of incomplete Astro Pi and ISS documentation (e.g., on the sensor orientation and magnetic environment of the station) and in separating the external (essentially geomagnetic) and internal (ISS generated) contributions in the Astro Pi magnetic field measurements. ISSB acquired significant expertise in the field of data in-flight calibration due to its involvement in the former INTERBALL program (magnetometer data, see e.g. [2]) and ESA's Cluster mission (magnetometer and plasma data, see [3–5]). Consequently, Andrei Ersen from the Narwhals team enrolled in an internship period at ISSB. The outcome of this collaboration went beyond its initial goal, suggesting the Astro Pi potential as magnetic field surveyor, with possible applications in, e.g., monitoring the magnetic field in the near-Earth environment.

Section 2 presents the Narwhals proposal, together with details about the Astro Pi measurements. Section 3 presents the assumptions and the method used to estimate the geomagnetic and ISS contributions to the observed magnetic field at Astro Pi location; the Narwhals

\* Corresponding author.

E-mail address: [blagau@spacescience.ro](mailto:blagau@spacescience.ro) (A. Blagau).

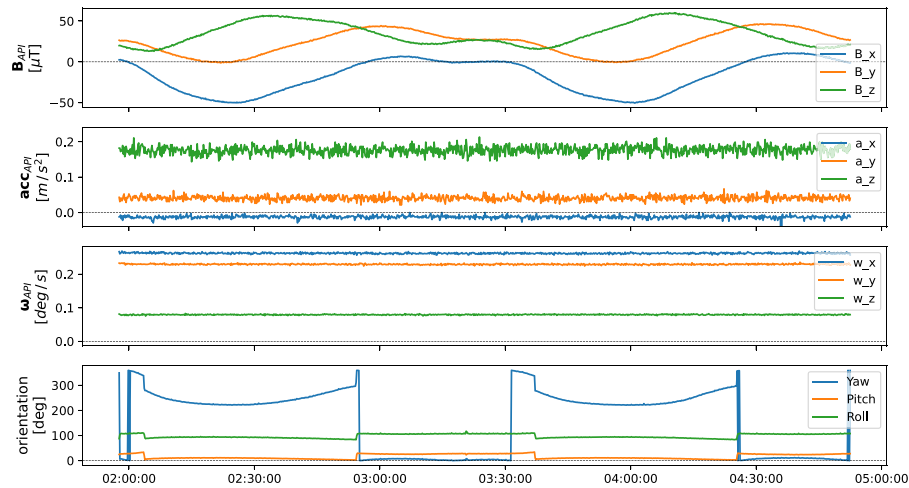


Fig. 1. Astro Pi (API) Sense HAT data. From top to bottom: magnetic field, acceleration and angular velocity, in the API reference frame. The bottom panel shows the API orientation (yaw, pitch, and roll Euler angles) derived from the three sensors' data by an onboard routine.

team findings are shown here as well. Using the same assumptions, in Section 4 a crude global representation of the geomagnetic field is provided, which is compared with the International Geomagnetic Reference Field (IGRF) model, and whose accuracy is discussed in some detail. The last section presents conclusions and prospects, including future possibilities to make systematic use of magnetic field observations onboard ISS.

## 2. Team Narwhals project

The Astro Pi kit consists of a credit-card size single-board computer (Raspberry Pi) with free operating system, and an add-on board, the Sense Hardware Attached on Top (HAT) made especially for the Astro Pi mission. The Sense HAT includes several sensors — gyroscope, accelerometer, magnetometer and sensors for temperature, pressure and humidity. A Python library provides access to the sensor's data. In what follows we are mainly interested in magnetometer data which, according to the specifications for similar sensors, available online (e.g. [6,7]), are observed with a typical resolution of  $\sim 3$  mGauss (300 nT). The gyroscope and accelerometer data will only be used in some consistency checks (see Section 3.4); according to the specifications, these sensors provide measurements in deg./s and, respectively, units of g.

The goal of the Narwhals project [8] was to evaluate the force and torque exerted by the geomagnetic field on ISS, seen as a magnetic object, and whether these can be used to maintain the orbit and the attitude of ISS (or of a low-orbit satellite, e.g. a cube-sat). If one considers the ISS as a magnetic body of moment  $\mathbf{m}$ , the force  $\mathbf{F}$  and torque  $\mathbf{N}$  exerted by the external (geomagnetic) field  $\mathbf{B}$  are ([9], Eqs. 5.69 and 5.71)

$$\begin{aligned} \mathbf{F} &= \nabla(\mathbf{m} \cdot \mathbf{B}) \\ \mathbf{N} &= \mathbf{m} \times \mathbf{B} \end{aligned} \quad (1)$$

After separating the external and internal parts in the Astro Pi magnetic field measurements, the idea was to estimate the ISS magnetic moment  $\mathbf{m}$  by considering its internal magnetic field  $\mathbf{B}_{\text{iss}}$  as the remnant field (or permanence) of a magnet with volume  $V_{\text{iss}}$ , i.e.

$$\mathbf{m}_{\text{iss}} \sim \mathbf{B}_{\text{iss}} V_{\text{iss}} / \mu_0 \quad (2)$$

In this particular case, if  $\mathbf{m}_{\text{iss}}$  is regarded as constant, and assuming also that electrical currents can be neglected,  $\nabla \times \mathbf{B} = 0$ , Eqs. (1) become (with  $\mathbf{l}$  the unit vector along  $\mathbf{B}_{\text{iss}}$ ):

$$\begin{aligned} \mathbf{F} &= (\mathbf{m}_{\text{iss}} \cdot \nabla) \mathbf{B} = \mathbf{m}_{\text{iss}} \partial \mathbf{B} / \partial l \\ \mathbf{N} &= \mathbf{m}_{\text{iss}} \times \mathbf{B} \end{aligned} \quad (3)$$

The data acquisition program of the Narwhals team was run on the Raspberry Pi computer onboard ISS for a roughly 3 h time-window, starting around 2021-04-22/01:57 UTC. During this interval, data provided by the gyroscope, accelerometer, and magnetometer were recorded with a 10 s cadence for later transmission to the ground. The output from an on-board routine which, based on these data, should supply the necessary information for attitude recovery, has been recorded as well. All these quantities are plotted in Fig. 1.

A major issue in the Astro Pi (API) experiment is the lack of proper documentation on how the sensors are actually working, what is the orientation of the API box with respect to the ISS frame and how does the on-board processing take place. The raw information provided by the magnetometer, accelerometer, and gyroscope (first three panels in Fig. 1) are presumably retrieved in the API frame, whereas the on-board routine which supplies the attitude information (the Euler angles yaw, pitch, and roll in the fourth panel of Fig. 1) is not open-source and the results look inconsistent. For example, even if one can instruct this routine to rely only on certain sensor or sensor combination, the output is basically the same. Note also that the Euler angles have discontinuities, although these are not present in the raw data used to calculate them. Moreover, it is not clear how the accelerometer readings are taken into account: on ground, the sensor is used to provide one direction in space (i.e. along the gravity vector), but for the nearly free fall motion of the ISS along the orbit, this information is not available. Similarly, there are no indications on how to interpret the gyroscope data and, later on in this paper (end of Section 3.4) evidence will be provided that these data are inconsistent. The problematic sensor information and inferred orientation was noticed also by other teams (e.g., [10]).

These difficulties prevented the Narwhals team to reliably separate the geomagnetic and ISS-generated magnetic field based on the Astro Pi attitude information, and prompted for a more rigorous approach. Nevertheless, the Narwhals team derived sufficiently accurate estimates of the attitude and magnetic field contributions to carry out their study, as detailed in Section 3.5.

## 3. Separating the magnetic field contributions

Even though the external, geomagnetic part of the observed magnetic field is accurately known by geomagnetic field models, in order to separate it from the observations one needs to address all data — observations, geomagnetic field model, and internal ISS contribution — in a common reference frame. As pointed out above, the observed magnetic field comes in the API reference frame, whose orientation

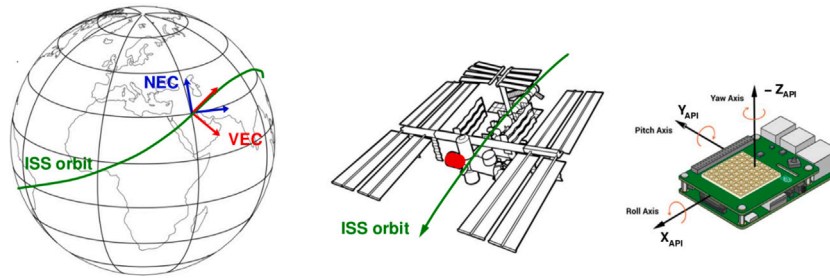


Fig. 2. Left: Orientation of NEC and VEC frames at one point along the ISS orbit. Their common Z axes is pointing to the Earth center. Center: ISS moving along the orbit, with the Columbus module in red. Right: Schematic view of the API board, together with API reference frame. (For interpretation of the references to colour in this figure legend, the reader is referred to the web version of this article.)

is not obvious. Deriving this orientation turned out to be a key step, initially addressed by the Narwhals team with the mathematical toolkit available at high school level (see Section 3.5). Later on, during the internship at ISSB, the matter was cast as an optimization problem and addressed, accordingly, by more advanced tools, as presented below.

The following reference frames will be used further on:

- **GEO** is the geographical geocentric frame, with the  $O_x$  axis in the Greenwich meridian plane,  $O_z$  the Earth rotation axis, and  $O_y$  completing the right system
- **NEC** (North East Center) frame is centered on ISS location. If  $\mathbf{r}$  is the position vector in the GEO frame, then  $\mathbf{e}_{\text{center}}$  is pointing toward Earth,  $-\mathbf{r}/|\mathbf{r}|$ ,  $\mathbf{e}_{\text{east}}$  toward the local East (along the vectorial product between  $\mathbf{e}_{\text{center}}$  and  $O_z$  axis in GEO) and  $\mathbf{e}_{\text{north}} = \mathbf{e}_{\text{east}} \times \mathbf{e}_{\text{center}}$ .
- **VEC** (Velocity East Center) frame is similar to NEC, i.e. they share the  $\mathbf{e}_{\text{center}}$  axis but  $\mathbf{e}_{\text{east}}$  is perpendicular to the orbital plane (not to the local meridian plane as in NEC) and  $\mathbf{e}_{\text{velocity}}$  completes the triad. For a satellite revolving on a circular orbit, like ISS,  $\mathbf{e}_{\text{velocity}}$  is along the velocity vector.
- **API** frame is linked to the Astro Pi sensor; its orientation is not known a priori.

The experimental setup is presented schematically in Fig. 2, showing the ISS orbit, together with the reference frames introduced above, i.e. NEC, VEC, and API.

### 3.1. Methodology and assumptions

The methodology outlined in this section relies on two main assumptions, namely that the orientation of Astro Pi sensors with respect to the ISS frame, as well as the magnetic field generated by ISS at the sensor location, are constant during the interval of analysis. Consequently, the contribution of ISS magnetic field can be modeled as a constant vector offset in the API frame.

Under nominal circumstances, i.e. apart from intervals reserved for maneuvers, the ISS attitude is maintained aligned along the **LVLH** (Local Vertical, Local Horizontal) frame. This means that ISS rotates along the pitch axis by  $\approx 4^\circ/\text{min}$ . (i.e. full rotation during an orbital period of  $\approx 90$  min.) to expose all the time the same face toward the Earth. Considering the geomagnetic field along the ISS orbit is reasonably well described by the available geomagnetic models, one can proceed as follows to separate the geomagnetic and ISS magnetic contributions in the Astro Pi measurements:

- compute the geomagnetic field model predictions along the ISS trajectory and transform those to the local VEC frame
- assuming that API measurements are the superposition of a constant (yet unknown) offset vector (ISS contribution) and the geomagnetic field, find the offset vector and the (constant) transformation from API to VEC by an optimization algorithm

- separate the geomagnetic and ISS generated field, evaluate the quality of results and, if possible, amend the underlying assumptions.

### 3.2. Geomagnetic field along ISS orbit

The ISS orbital elements at some specific times are captured in the so-called NORAD Two-Line Element (TLE) data set. Based on that and using a mathematical model which takes into account various perturbations (Earth's oblateness, atmospheric drag, gravitational influence from Sun and Moon etc.) the ISS position and velocity valid for a certain time epoch are predicted. The approximate TLE values were provided in the Astro Pi records but the present analysis uses the refined TLE, publicly available [11]. To further compute the ISS trajectory we used the Skyfield Python package [12,13], which offers a precision of  $\sim 10^{-2}$  m in vector position. The first two panels in Fig. 3 present the evolution of ISS position and, respectively, velocity in the geographic (Earth fixed) frame.

To obtain the geomagnetic field along the ISS trajectory we used the CHAOS-7.8 field model [14], valid up to 30th June 2021. The model coefficients and a Python package to compute NEC magnetic components at a certain position and time are available online [15]. The third panel in Fig. 3 presents the CHAOS geomagnetic field NEC components at ISS location. As one can observe, the aspect is very different when compared with the magnetic field recorded by API sensor (first panel in Fig. 1); it is the task of the next two sections to clarify this aspect and present both the observed magnetic field and the geomagnetic field model in a common reference frame.

### 3.3. Problem optimization

To get a hint on the internal field produced by ISS, the first panel in Fig. 4 shows the module of the magnetic field recorded by API and that of the geomagnetic field, i.e. quantities which do not depend on the reference frame. It turns out that ISS produces a magnetic field comparable in magnitude, i.e. tens of  $\mu\text{T}$ .

The optimization problem outlined in Section 3.1 recommends VEC as the working reference frame. Considering first the geomagnetic field, given in NEC, a transformation to VEC implies a simple yaw rotation of angle  $\theta$  around the common  $\mathbf{e}_{\text{center}}$  direction:

$$\mathbf{M}_{\text{NEC} \rightarrow \text{VEC}}(t_i) = \begin{bmatrix} \cos \theta(t_i) & \sin \theta(t_i) & 0 \\ -\sin \theta(t_i) & \cos \theta(t_i) & 0 \\ 0 & 0 & 1 \end{bmatrix} \quad (4)$$

where  $i = 1 \dots N$  designates the time-tags of our  $N$  measurements. The angle is obtained from the components of ISS velocity in the tangential plane (plane perpendicular to  $\mathbf{e}_{\text{center}}$ ), namely as

$$\theta(t_i) = \arctan(\cos(\text{Lat}_i) \cdot \delta \text{Lon}_i / \delta \text{Lat}_i) \quad (5)$$

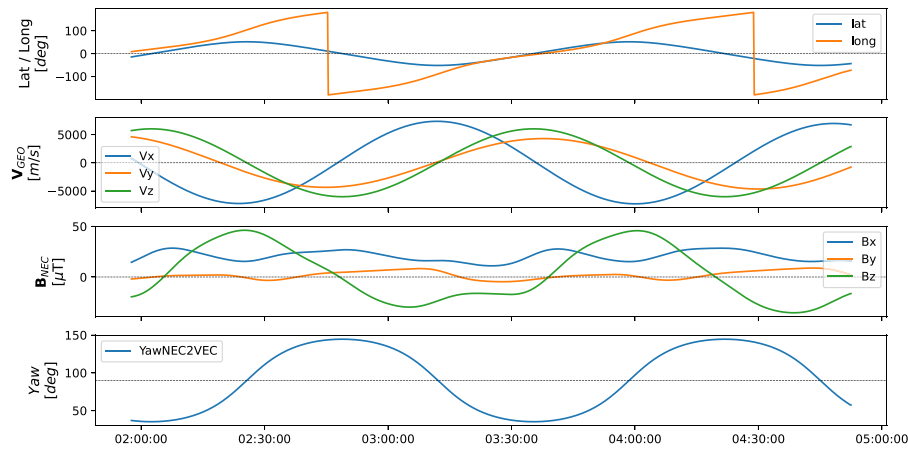


Fig. 3. ISS trajectory and geomagnetic field data. From top to bottom: ISS latitude and longitude, ISS velocity in geographic coordinates, geomagnetic field components in NEC along ISS orbit, and yaw rotation angle from NEC to VEC (around the common axis, pointing to the Earth center).

with  $\delta$  indicating the time variation and  $\text{Lat}_i$ ,  $\text{Lon}_i$  the latitude and, respectively, longitude at  $t_i$ . Its evolution is presented in the last panel of Fig. 3.

As for the magnetic field measured by API, a general rotation to VEC frame by yaw angle  $\alpha$ , then pitch angle  $\beta$ , and then roll angle  $\gamma$  implies a rotation matrix

$$\mathbf{M}_{\text{API2VEC}} = \begin{bmatrix} 1 & 0 & 0 \\ 0 & \cos\gamma & \sin\gamma \\ 0 & -\sin\gamma & \cos\gamma \end{bmatrix} \begin{bmatrix} \cos\beta & 0 & -\sin\beta \\ 0 & 1 & 0 \\ \sin\beta & 0 & \cos\beta \end{bmatrix} \begin{bmatrix} \cos\alpha & \sin\alpha & 0 \\ -\sin\alpha & \cos\alpha & 0 \\ 0 & 0 & 1 \end{bmatrix} = \begin{bmatrix} \cos\beta \cos\alpha & \cos\beta \sin\alpha & -\sin\beta \\ \sin\beta \cos\alpha \sin\gamma - \sin\alpha \cos\gamma & \sin\beta \sin\alpha \sin\gamma + \cos\alpha \cos\gamma & \cos\beta \sin\gamma \\ \sin\beta \cos\alpha \cos\gamma + \sin\alpha \sin\gamma & \sin\beta \sin\alpha \cos\gamma - \cos\alpha \sin\gamma & \cos\beta \cos\gamma \end{bmatrix} \quad (6)$$

The optimization problem seeks to find the angles  $\alpha$ ,  $\beta$ ,  $\gamma$ , as well as the offset vector  $\mathbf{b}$  (six parameters in total) by minimizing the quantity

$$\sum_{i=1}^N \|\mathbf{M}_{\text{NEC2VEC}}(t_i) \mathbf{B}^{\text{CHAOS}}(t_i) - \mathbf{M}_{\text{API2VEC}}(\mathbf{B}^{\text{API}}(t_i) - \mathbf{b})\|^2 \quad (7)$$

where  $\|\dots\|$  designates vector module. Here  $\mathbf{B}^{\text{CHAOS}}(t_i)$  and  $\mathbf{B}^{\text{API}}(t_i)$  represent the geomagnetic field model (originally in NEC frame) and, respectively, the magnetic field measured by API (originally in API frame) at time  $t_i$ . The terms of the sum in Eq. (7) are magnetic residues, i.e. differences between the model predictions,  $\mathbf{B}^{\text{CHAOS}}(t_i)$ , and the geomagnetic field measured by API, namely  $\mathbf{B}^{\text{API}}(t_i) - \mathbf{b}$ , transformed to a common reference frame (here VEC). Numerically, the six parameters are obtained by using the `curve_fit` function, part of the `scipy.optimize` Python package, which uses a non-linear least squares algorithm.

### 3.4. Results and consistency checks

The minimization from Eq. (7) turns to be stable, basically independent on the initial guess supplied to the `curve_fit` algorithm, resulting in a vector offset  $\mathbf{b} \sim [5.6, -12.1, -37.6]$   $\mu\text{T}$  in API frame, or  $[38.6, 4.0, -9.2]$  in VEC.  $\mathbf{Z}_{\text{API}}$  is oriented roughly anti-parallel to  $\mathbf{X}_{\text{VEC}}$ , i.e. making an angle of  $\sim 158^\circ$ , while the  $\mathbf{X}_{\text{API}}$  and  $\mathbf{Y}_{\text{API}}$  axes are roughly at  $45^\circ$  from the  $-\mathbf{Z}_{\text{VEC}}$  and, respectively,  $-\mathbf{Y}_{\text{VEC}}$  directions. In the VEC frame, after removing the offset, the component by component differences (residues) between API measurements and CHAOS geomagnetic field are presented in the second panel of Fig. 4.

To further reduce the residues, we allow for periodic variations in the Euler angles  $\alpha$ ,  $\beta$ , and  $\gamma$  from Eq. (6), with frequencies linked to the

ISS orbital period. More specifically, we modeled

$$\begin{aligned} \alpha(t_i) &= \alpha_0 + A_\alpha^1 \sin(\omega t_i + \phi_\alpha^1) + A_\alpha^2 \sin(2\omega t_i + \phi_\alpha^2) \\ \beta(t_i) &= \beta_0 + A_\beta^1 \sin(\omega t_i + \phi_\beta^1) + A_\beta^2 \sin(2\omega t_i + \phi_\beta^2) \\ \gamma(t_i) &= \gamma_0 + A_\gamma^1 \sin(\omega t_i + \phi_\gamma^1) + A_\gamma^2 \sin(2\omega t_i + \phi_\gamma^2) \end{aligned} \quad (8)$$

with  $\omega$  as extracted from the TLE data. Physically, these corresponds to the (always present) small yaw, pitch and roll oscillations in ISS orientation due to the way the Space Station's attitude controllers (thrusters, gyroscopes) work in practice. The minimization problem seeks now for 18 parameters (3 for the components of  $\mathbf{b}$  and 5 for each of the Euler angles).

The results provided by `curve_fit` in this case, presented in the third panel of Fig. 4, proved to be stable as well. The residues decreased significantly, to around 0.5  $\mu\text{T}$  rms on each component, close to the resolution offered by the API magnetic sensor. At the same time, the amplitude of variation in  $\alpha$ ,  $\beta$ , and  $\gamma$  are indeed small (average value of all amplitudes in Eqs. (8) is  $\sim 6^\circ$ ) and the new components of the offset  $\mathbf{b}$  in API frame, i.e.  $[4.0, -10.7, -38.1]$   $\mu\text{T}$ , are close to the case of fixed Euler angles. These aspects are all strong indications of a good physical modeling and of a reliable methodology to estimate the ISS internal field.

An additional confirmation is offered by the accelerometer data; the components of acceleration in VEC frame, presented in the fourth panel of Fig. 4, show that this vector is contained in the orbital plane, as expected. Indeed, the accelerometer readings should detect the influence of atmospheric drag, directed oppositely to the orbital velocity. Additionally, a sensor placed at a certain distance from the center of mass will record an acceleration due to the forces that maintain ISS orientation; in the first approximation (i.e. neglecting the small variation in attitude) these forces lay in the orbital plane as well.

The TLE data allow us to roughly estimate the acceleration due to the atmospheric drag. Indeed, one orbital parameter is the so-called ballistic coefficient, or first derivative of mean motion, defined as the daily rate of change in the number of orbits the satellites completes each day, divided by 2. For our specific event, this provides an acceleration of the order of  $0.003 \text{ mm/s}^2$ . At the same time, keeping the ISS orientation aligned along the local LVLH frame, implies an angular acceleration given by the orbital motion, i.e.  $\omega = 0.0011 \text{ rad/s}$  in our case. By considering a distance of 10 m between the sensor location and the ISS center of mass, this leads us to an acceleration of the order of  $0.012 \text{ mm/s}^2$ . These evaluations would be relatively close to the API data if the sensor readings are also provided in  $\text{mm/s}^2$  and not in g's, as mentioned in the specifications (see Section 2).



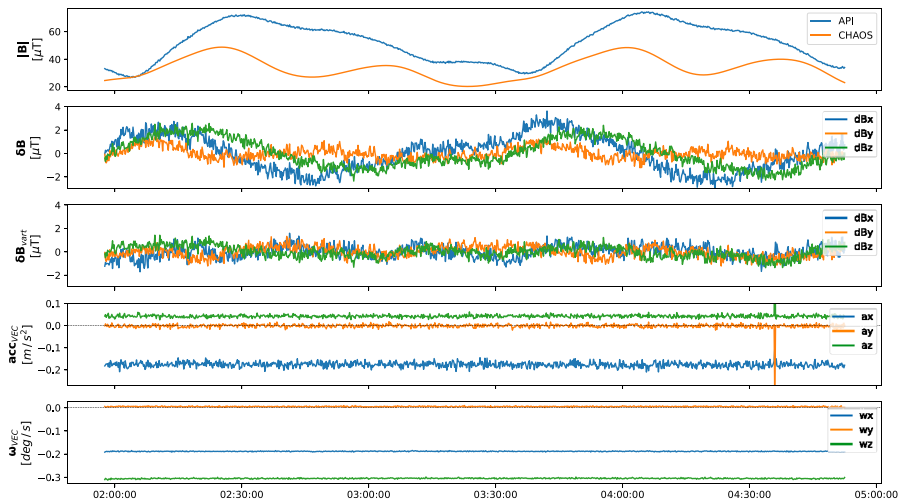


**Fig. 4.** Residues and cross-checks. From top to bottom: modules of the magnetic field observed by API (blue) and of the model geomagnetic field (orange), residual magnetic field after simpler optimization (6 parameters), and after more complex optimizations (18 parameters), API acceleration, and API angular velocity. The components of the magnetic field residuals, acceleration, and angular velocity are presented in VEC. (For interpretation of the references to colour in this figure legend, the reader is referred to the web version of this article.)

**Table 1**

Results of applying the optimization problem to API data when the CHAOS magnetic model is taken as reference (first two lines) and when API based global magnetic field models are derived as described in Section 4 (the following three lines). The offset vector in the API frame and the rms of magnetic residues along the ISS trajectory in the VEC frame are both indicated. The last two lines present the magnetic differences in IGRF13 model predictions along the ISS trajectory when only terms corresponding to  $n = 4$  and, respectively,  $n = 4$  together with  $n = 5$ , are considered.

	Euler angles	Offset in API [ $\mu\text{T}$ ]				residues in VEC [ $\mu\text{T}$ ]			
		$b_x$	$b_y$	$b_z$	$  b  $	$r_x$	$r_y$	$r_z$	$  r  $
Data vs. CHAOS	Fixed	5.6	-12.1	-37.6	39.9	1.46	0.49	1.20	1.95
Data vs. CHAOS	Variable	4.0	-10.7	-38.1	39.8	0.53	0.46	0.49	0.86
Data vs. AstroPi1						5.15	6.21	5.72	9.89
Data vs. AstroPi2	Fixed	6.6	-12.5	-37.3	39.8	1.13	0.95	1.32	1.98
Data vs. AstroPi3	Variable	6.1	-12.2	-36.3	38.7	0.69	0.59	0.92	1.29
IGRF13, $n = 4$						0.99	0.94	1.52	2.04
IGRF13, $n = 4, 5$						1.07	0.99	1.63	2.19

As for the gyroscope readings, (fifth panel in Fig. 4), both the orientation and the magnitude of  $\omega_{\text{gyro}}$  vector, i.e.  $\sim 0.36$  deg/s normal to  $e_{\text{east}}$ , appear to be wrong. Indeed, the main orientation of  $\omega_{\text{gyro}}$  should be along  $e_{\text{east}}$  in VEC frame, whereas the magnitude should be close to the angular velocity imposed by the orbital motion and attitude control, i.e.  $2\omega \sim 0.0022$  rad/s  $\sim 0.13$  deg/s. As mentioned in Section 2, other Astro Pi teams arrived at the same conclusion by analyzing their data.

The results of applying the optimization problem to API data, using the CHAOS magnetic field model as reference, are presented in the first two lines of Table 1.

### 3.5. Team Narwhals results

Using a much simpler approach, based on educated guess together with trial and error, team Narwhals managed to obtain rather good results on the API orientation and on the ISS magnetic field offset, i.e. the key elements in further assessing the force and the torque on ISS due to the geomagnetic field [8]. First, the geomagnetic field model was computed in VEC, using a procedure very much alike the one outline at the beginning of Section 3.3. Then, the team observed similar evolution (i.e. amplitude and phase) for magnetic field measurements along  $-Z_{\text{API}}$  and for geomagnetic field model along  $X_{\text{VEC}}$ , and therefore assumed the two directions roughly coincide. Finally, the team rotated the API board in small steps around the such guessed axis, until the

components of the observed magnetic field were essentially similar, but shifted, with respect to the components of the geomagnetic field model, as shown in the first three panels of Fig. 5. The average of the (more or less) constant magnetic field offset, derived by subtracting the model from the observed field (see the last panel), provided a proxy for the proper magnetic field of the station,  $B_{\text{ISS}}$ . Quantitatively,  $B_{\text{ISS}}$  in VEC is  $\sim [39.3, 4.8, -4.0]$   $\mu\text{T}$ , in reasonable agreement with the offset  $b$  derived in Section 3.3 for the case of constant Euler angles, namely  $[38.6, 4.0, -9.2]$   $\mu\text{T}$ .

Assuming for simplicity an ISS magnetic field of  $\sim 40$   $\mu\text{T}$  (absolute value) and a volume of  $\sim 1000$   $\text{m}^3$  [16], Eq. (2) provides a magnetic moment of the station  $m_{\text{ISS}} \sim 3 \cdot 10^4$   $\text{Am}^2$ , oriented essentially along the station velocity. While the exact value of the magnetic field derivative along the ISS magnetic moment direction depends on the station location (e.g., some  $55^\circ$  with the latitude circle at equator and parallel to the latitude circle at the extreme northern and southern points), its order of magnitude is  $||B||/r$ , with  $||B||$  less than 50  $\mu\text{T}$  and  $r \sim 6700$  km. Consequently,  $\partial B/\partial l$  in Eqs. (3) is less than  $10^{-11}$  T/m, yielding the force of the order of  $3 \cdot 10^{-7}$  N. Considering the mass of ISS of some  $4 \cdot 10^5$  kg [16], the related acceleration is of the order of  $10^{-12}$   $\text{m/s}^2$ , much smaller than the acceleration due to the atmospheric drag of  $\sim 3 \cdot 10^{-6}$   $\text{m/s}^2$  (see above).

At the same time, Eqs. (3) provide a torque of  $\sim 1$  Nm; if we (coarsely) model the mass distribution of ISS by that of a sphere having a radius of  $\sim 10$  m, one arrives at an angular acceleration of some  $\sim 10^{-7}$   $\text{m/s}^2$ . Considering the linear size of ISS of  $\sim 100$  m [16], the uneven mass distribution, and the tensorial character of the inertia moment, the error margin of this estimate is probably an order of magnitude or so. By comparing, again, with the estimate above and with the accelerometer data, the torque is obviously much more effective in impacting the ISS dynamics.

Team Narwhals has also checked the force and the torque caused by the interaction of the geomagnetic field with the magnetic moment of a coil, be it driven passively by induction due to the variation of the geomagnetic field along the orbit, or actively by a (significant) current through the coil. In both cases, and for a couple of coil specifications — appropriate for ISS or for smaller platforms, like CubeSat — the results were similar, namely that force impact is typically (much) smaller than that of the atmospheric drag (except for superconducting coils, as yet unrealistic on orbit), whereas the torque can result in a significant effect.

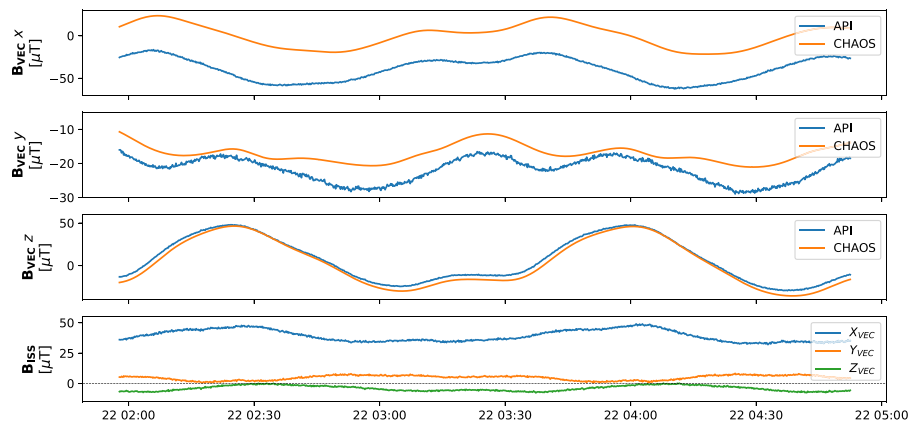


Fig. 5. Team Narwhals results. The first three panels present the X, Y, and Z components of geomagnetic field model (orange) and API measurements (blue) rotated in VEC, as obtained by the Narwhals team. The component by component difference between these quantities is presented in the last panel. Adjusted from the Report presented by team Narwhals. (For interpretation of the references to colour in this figure legend, the reader is referred to the web version of this article.)

#### 4. Global geomagnetic field based on Astro Pi data

(11)

The ESA's Astro Pi Challenge is an educational project intended to inspire and attract young people to the field of space science. Inevitably, the hardware involved is by no means designed for a proper scientific investigation. Nevertheless, the use of this kind of simple, relatively inexpensive sensors to monitor the magnetic field (both the internal and external part) at ISS has a great potential. To give an example that illustrates this aspect, we will derive a simple global model of the geomagnetic field using exclusively the Astro Pi measurements acquired on just two orbits, i.e. the data shown in the first panel of Fig. 1, and compare it with (a reduced version of) the 13<sup>th</sup> generation of the International Geomagnetic Reference Field (IGRF, [17]). In this regard, we mention that Team Mag-AZ, from the same 2020/21 edition of Astro Pi Challenge, tried as well to reconstruct the geomagnetic field based on ISS observations, though they have not considered the ISS proper field (see below) and the errors were accordingly large, comparable to the geomagnetic field itself [10]. In a recent arXiv manuscript [18], Team Mag-AZ used a larger data set (10 ISS orbits) which reduced the errors to an estimated level of 10% in the dipole component and improved also their multipolar expansion up to order 3. However, the large disagreement between the model field and the field observed along each orbit remained difficult to explain, as pointed out in the Conclusions of [18].

Considering a spherical coordinate system centered on Earth, with  $r$  the distance from Earth center,  $\theta$  the co-latitude (i.e.  $\pi/2$  - latitude), and  $\phi$  the longitude, the geomagnetic field vector  $\mathbf{B}(r, \theta, \phi)$  can be obtained from the potential function  $V(r, \theta, \phi)$  as

$$\mathbf{B} = -\nabla V = -\left( \frac{\partial V}{\partial r} \mathbf{e}_r + \frac{1}{r} \frac{\partial V}{\partial \theta} \mathbf{e}_\theta + \frac{1}{r \sin(\theta)} \frac{\partial V}{\partial \phi} \mathbf{e}_\phi \right) \quad (9)$$

where  $\mathbf{e}_r$ ,  $\mathbf{e}_\theta$ , and  $\mathbf{e}_\phi$  are unit vectors in the local radial, meridional, and azimuthal directions, respectively.

One uses the well known representation of  $V(r, \theta, \phi)$  as a finite series of spherical harmonics functions (see e.g. [17])

$$V(r, \theta, \phi) = a \sum_{n=1}^N \sum_{m=0}^n \left( \frac{a}{r} \right)^{n+1} [g_n^m \cos(m\phi) + h_n^m \sin(m\phi)] P_n^m(\cos(\theta)) \quad (10)$$

where  $a$  designates the Earth radius and  $g_n^m$ ,  $h_n^m$  are the so-called Gauss coefficients. The  $P_n^m$  polynomial functions are Schmidt semi-normalized associated Legendre functions of degree  $n$  and order  $m$  [19], given by

$$P_n^m(x) = \begin{cases} \frac{1}{2^n n!} \left( \frac{d}{dx} \right)^n (x^2 - 1)^n & \text{when } m = 0 \\ \frac{1}{2^n n!} \sqrt{2} \frac{(n-m)!}{(n+m)!} (1-x^2)^{m/2} \left( \frac{d}{dx} \right)^{n+m} (x^2 - 1)^n & \text{when } m \neq 0 \end{cases}$$

In what follows, one limits the description of geomagnetic field up to the spherical harmonics of degree  $n_{\max} = 3$ . In that respect, one notes that for  $n \geq 5$  all Gauss coefficients in the IGRF model [17] are essentially smaller than 300 nT, i.e. the resolution provided by the Astro Pi magnetometer, and therefore it is unrealistic to use a series expansion beyond that degree. When  $n_{\max} = 3$ , algebraic expressions for the potential function  $V(r, \theta, \phi)$  and the associated magnetic field  $\mathbf{B}(r, \theta, \phi)$  are provided in Appendix. The correctness of these expressions has been confirmed numerically using a Python based package [20] that calculates IGRF model predictions.

The 15 Gauss coefficients  $g_1^0, g_1^1, h_1^1, \dots, g_3^3, h_3^3$ , together with the parameters that describe the ISS orientation and, possibly, its internal field, can be obtained self-consistently from an optimization problem, similarly to the procedure presented in Section 3.3. To that end, in Eq. (7), instead of  $\mathbf{B}^{\text{CHAOS}}$  one will now use a magnetic field model representation with  $n_{\max} = 3$ , that depends on the 15 Gauss coefficients as detailed in Appendix. Three cases were analyzed, (i) when the ISS-generated field is neglected; then only an additional set of 3 parameters, i.e. the yaw, pitch, and roll angles for API2VEC rotation, are needed, (ii) when also the offsets produced by ISS field are considered, that implies 3 more parameters in the optimization problem, and (iii) when the magnetic offsets as well as the more complex ISS yaw, pitch, and roll motion described by Eqs. (8) have been considered (33 parameters in total, coming from 15 Gauss coefficients, 15 parameters in Eqs. (8) and 3 parameters for the vector offset  $\mathbf{b}$ ).

The magnetic residues (i.e. differences between the measured and the self-consistently obtained geomagnetic models) in each of the three cases are presented in Fig. 6. As can be seen from the first two panels, taking into account and removing the ISS generated field has a major impact on reducing the residues. The residues decline further when also the oscillations in yaw, pitch, and roll are considered (see the third panel). It is worth mentioning that the components of the newly obtained ISS offsets are close to those obtained in Section 3.4, e.g. [6.1, -12.2, -36.2]  $\mu\text{T}$  in API frame for the case presented in the third panel. Moreover, the results were remarkably stable, basically independent on the initial guess supplied to the curve\_fit algorithm.

In Fig. 7, maps of global magnetic field intensity (color coded) and magnitude of horizontal component (contour lines) are presented. The upper left shows the (13<sup>th</sup> generation of) IGRF model for  $n_{\max} = 3$  (IGRF <sub>$n_{\max}=3$</sub> ), based on the Gauss coefficients from [17]. The upper right, i.e. geomagnetic model named AstroPi1, corresponds to the situation when the ISS magnetic field is not separated from Astro Pi measurements, and only constant Euler angles for API2VEC rotation

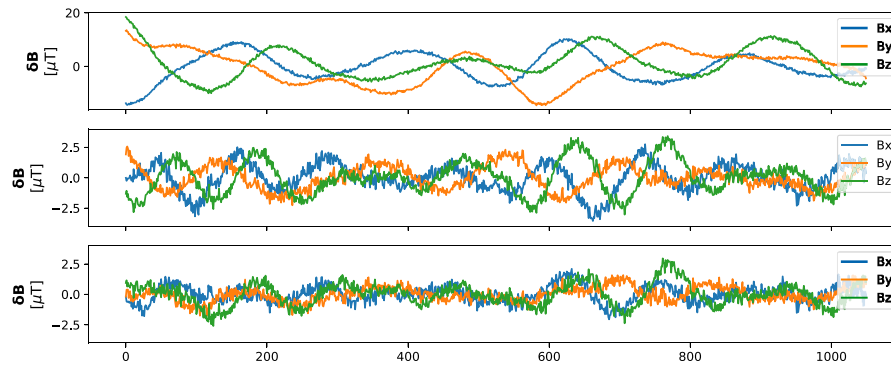


**Fig. 6.** The differences between the Astro Pi measurements and the Astro Pi based geomagnetic models in three cases: when constant Euler angles for ISS orientation but no ISS-generated field are considered (top), and when constant (middle) or slightly variable (bottom) Euler angle, together with a (constant) ISS-generated field are considered. The components of the magnetic field residuals are presented in **VEC**.

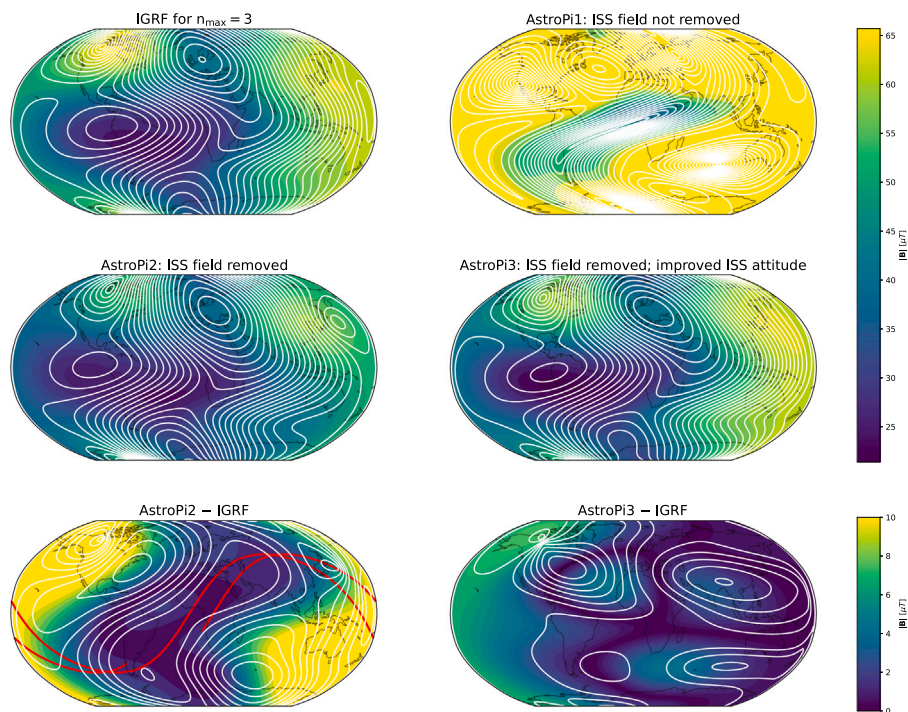


**Fig. 7.** Global maps of magnetic field module (color coded) and module of horizontal component (contour lines) for IGRF <sub>$n_{\max}=3$</sub>  (top left) and the three Astro Pi based geomagnetic models described in the text (top right and middle plots). At the bottom, the (absolute) difference between IGRF <sub>$n_{\max}=3$</sub>  and the AstroPi2 (left) and AstroPi3 (right) geomagnetic models are presented. The ISS orbit (red) is overlaid on the bottom left plot. See more text for explanations. (For interpretation of the references to colour in this figure legend, the reader is referred to the web version of this article.)

are considered. When, in addition, the ISS-induced field is modeled as constant magnetic offsets, one obtains the middle left plot, i.e. geomagnetic model named AstroPi2, which is more similar to the reference IGRF <sub>$n_{\max}=3$</sub>  map. Finally, the resemblance is significantly better when the ISS small oscillations in yaw, pitch and roll motion are considered, see the middle right plot, i.e. geomagnetic model named AstroPi3. The same color scale, indicated on the far right in Fig. 7, has been used in all these plots.

To quantify the mismatch between the IGRF <sub>$n_{\max}=3$</sub>  and the Astro Pi based models, the average (absolute) difference in total magnetic intensities has been computed, yielding  $\sim 38.2 \mu\text{T}$  for AstroPi1,  $\sim 5.5 \mu\text{T}$  for AstroPi2, and  $\sim 2.4 \mu\text{T}$  for AstroPi3. Note that the total magnetic intensities for IGRF <sub>$n_{\max}=3$</sub>  varies between 23.6 and 65.7  $\mu\text{T}$ , with an average value of 45.5  $\mu\text{T}$ . (Since our computations were based on

regular latitude-longitude grids, putting thus more weight on the polar regions, we are aware that these numbers are rough estimates.) The lower left/right part in Fig. 7 presents the (absolute) difference in magnetic field intensity (color coded) and magnitude of horizontal component (contour lines) between IGRF <sub>$n_{\max}=3$</sub>  and AstroPi2/AstroPi3 model. The same color scale, indicated on the bottom far right, has been used for these two plots.

The results of applying the optimization problem to API data obtained in this section, i.e. the offset vector in the **API** frame and the rms of magnetic residues along the ISS trajectory in the **VEC** frame, are summarized in lines 3–5 from Table 1. The last two lines from Table 1 present the magnetic differences in IGRF13 model predictions along the ISS trajectory when only terms corresponding to  $n = 4$  and, respectively,  $n = 4$  together with  $n = 5$ , are considered (the

differences have been computed with the same software package [20] used to numerically validate the expressions in the Appendix. One could interpret the residues obtained in Section 3.4 for the case of slowly varying Euler angles (line 2 in Table 1), with magnitude of  $0.86 \mu\text{T}$ , as an overall limitation due to the experimental set-up (sensor precision, calibrations) and the method (physical modeling, numerical approach). If one looks at the differences due to the contributions from  $n = 4$  in the IGRF13 magnetic model (line 6 in Table 1), with magnitude of  $2.04 \mu\text{T}$ , one could further speculate that some small improvement of the API based global model is still possible by using a representation for the geomagnetic field up to  $n_{\max}=4$  in the spherical harmonics, instead of  $n_{\max}=3$ , as done above. Going one degree further, to order 5, would add just another  $0.15 \mu\text{T}$  to the magnetic field magnitude (compare the last two lines in Table 1) and would probably bring no further improvements. This also confirms the point made above, that expansions to orders  $\geq 5$  would not help, given the limited resolution,  $\sim 0.3 \mu\text{T}$ , of the Astro Pi sensor.

## 5. Prospects and conclusions

The original proposal of Team Narwhals addressed the magnetic field observations mainly at operational level, as a mean to assess the ISS dynamics due to the force and torque exerted by the ISS interaction with the geomagnetic field. While that task was a valuable learning experience for Team Narwhals, it turned out that magnetic observations made by cheap, off-the-shelf magnetic field sensors onboard ISS have a great potential, as proved by our decent estimates on the geomagnetic field and ISS proper field.

In the minimization problem used above, most of the parameters were cast to model the attitude of the Astro Pi sensor. By using better sensors with known orientation and improved measurements' accuracy, at a modest price compared to the overall expenses of the ISS program, one could target various applications, of which a few are commented below. For the time being, this is essentially done at conceptual level, without a quantitative assessment of the actual potential costs involved. While we are aware that improving the accuracy of the measurements depends not just on the quality of the sensor(s), but also on overcoming the significant difficulty of the magnetic 'dirty' environment onboard ISS, recent results with other 'dirty' platforms are encouraging (even though these are much smaller satellite platforms).

One recent example is the Service Oriented Spacecraft Magnetometer (SOSMAG) instrument [21] onboard the Korean geostationary satellite GeoKomsat-2 A (GK2 A). Advanced data processing techniques, as applied in [22] – in this case to AC magnetic field observations – could correct various disturbing effects down to less than or around 1 nT, as required by the space weather monitoring purpose of the instrument. The measurement requirements for space weather application based on Low Earth Orbit satellites, like ISS, are less strict, e.g. being roughly at the order of 10 nT for monitoring geomagnetic pulsations or 100 nT, for monitoring magnetospheric currents [23]. Since systematic satellite observations are not available at such low altitudes as of ISS, properly processed ISS data may already make a useful contribution to space weather monitoring.

In the last years, there is a growing interest in using data from the so called 'platform magnetometers', i.e. magnetometers originally not designed for scientific investigations but mainly used as part of the attitude control system. See in that respect the effort in calibrating and interpreting data from IRIDIUM [24], DMSP [25], CryoSat-2 [26] or GRACE [27] satellites. As an example, CryoSat-2 measurements were used in improving the geomagnetic field model by filling the gap between data provided by dedicated magnetic field missions, i.e. between the end of CHAMP (2010) and the start of Swarm (2013) [28], in studies on magnetospheric ring current [26] or in probing the electrical conductivity of the mantle [29]. By upgraded sensors and development of adequate data processing routines, perhaps something similar could

be done also with data collected by ISS — whose altitude is lower than both Swarm and CryoSat.

Last but not least, separating the observations onboard ISS into geomagnetic and ISS proper field, could also be of help to some of the various experiments onboard ISS. Personal communication with ESA staff, including electromagnetic compatibility (EMC) experts, indicate that good knowledge of the local magnetic environment would be indeed highly desirable for certain experiments, some of which require quiet magnetic conditions.

## CRedit authorship contribution statement

**Adrian Blagau:** Developed the optimization method and included the small changes in the ISS attitude along the orbit, Involved in data analysis and interpretation and guided Andrei Ersen during his internship at ISSB, Writing – original draft. **Andrei Ersen:** Proposed and lead the activities carried-out under Astro Pi Challenge, Involved in data analysis and interpretation, Writing – original draft. **Corina Dobrescu:** Supervised Andrei Ersen from hands-on Astro Pi session to theory and data programming, Writing – original draft. **Octav Marghitu:** Foresaw the possibility to use Astro Pi as magnetic field surveyor in the early phase of the work, Involved in data analysis and interpretation and guided Andrei Ersen during his internship at ISSB, Writing – original draft.

## Declaration of competing interest

The authors declare that they have no known competing financial interests or personal relationships that could have appeared to influence the work reported in this paper.

## Acknowledgments

Dr. Atul Deep and his ESA colleagues provided useful information on the specifications of ISS magnetic field.

## Funding

The work at the Institute for Space Sciences, Bucharest, was supported by the European Space Agency project MAGICS, PRODEX contract 4000127660.

## Appendix

Considering the Schmidt semi-normalized Legendre function in Eqs. (11), the expression for  $V(r, \theta, \phi)$  in Eq. (10) takes the following form when  $n_{\max} = 3$

$$\begin{aligned} V(r, \theta, \phi) = & \frac{a^3}{r^2} \left\{ g_1^0 \cos(\theta) + [g_1^1 \cos(\phi) + h_1^1 \sin(\phi)] \sin(\theta) \right\} + \\ & \frac{a^4}{r^3} \left\{ g_2^0 \left( 1 - \frac{3}{2} \sin^2(\theta) \right) + \sqrt{3} [g_2^1 \cos(\phi) + h_2^1 \sin(\phi)] \sin(\theta) \cos(\theta) \right. \\ & \left. + \frac{\sqrt{3}}{2} [g_2^2 \cos(2\phi) + h_2^2 \sin(2\phi)] \sin^2(\theta) \right\} + \\ & \frac{a^5}{r^4} \left\{ g_3^0 \cos(\theta) \left( 1 - \frac{5}{2} \sin^2(\theta) \right) + \right. \\ & \sqrt{\frac{3}{2}} [g_3^1 \cos(\phi) + h_3^1 \sin(\phi)] \sin(\theta) \left( 2 - \frac{5}{2} \sin^2(\theta) \right) + \\ & \sqrt{\frac{15}{4}} [g_3^2 \cos(2\phi) + h_3^2 \sin(2\phi)] \cos(\theta) \sin^2(\theta) \\ & \left. + \sqrt{\frac{5}{8}} [g_3^3 \cos(3\phi) + h_3^3 \sin(3\phi)] \sin^3(\theta) \right\} \end{aligned}$$

Based on Eq. (9), one obtains the following expression for magnetic field vector, where the brackets in the sum corresponds to  $n = 1, n = 2,$



and  $n = 3$ , respectively:

$$\mathbf{B}_{n_{\max}=3} = \begin{bmatrix} B_r \\ B_\theta \\ B_\phi \end{bmatrix}_{n_{\max}=3} = \begin{bmatrix} \frac{2}{r^3} \{ g_1^0 \cos(\theta) + [g_1^1 \cos(\phi) + h_1^1 \sin(\phi)] \sin(\theta) \} \\ -\frac{a^3}{r^3} \{ -g_1^0 \sin(\theta) + [g_1^1 \cos(\phi) + h_1^1 \sin(\phi)] \cos(\theta) \} \\ -\frac{a^3}{r^3} \frac{1}{\sin(\theta)} \{ [-g_1^1 \sin(\phi) + h_1^1 \cos(\phi)] \sin(\theta) \} \end{bmatrix} + \begin{bmatrix} 3 \frac{a^4}{r^4} \left\{ g_2^0 \left( 1 - \frac{3}{2} \sin^2(\theta) \right) + \sqrt{3} [g_2^1 \cos(\phi) + h_2^1 \sin(\phi)] \sin(\theta) \cos(\theta) \right. \right. \\ \left. \left. + \frac{\sqrt{3}}{2} [g_2^2 \cos(2\phi) + h_2^2 \sin(2\phi)] \sin^2(\theta) \right\} \\ -\frac{a^4}{r^4} \left\{ -3g_2^0 \sin(\theta) \cos(\theta) + \sqrt{3} [g_2^1 \cos(\phi) + h_2^1 \sin(\phi)] \cos(2\theta) \right. \\ \left. + \sqrt{3} [g_2^2 \cos(2\phi) + h_2^2 \sin(2\phi)] \sin(\theta) \cos(\theta) \right\} \\ \left. -\frac{a^4}{r^4} \frac{1}{\sin(\theta)} \left\{ \sqrt{3} [-g_2^1 \sin(\phi) + h_2^1 \cos(\phi)] \sin(\theta) \cos(\theta) \right. \right. \\ \left. \left. + \sqrt{3} [-g_2^2 \sin(2\phi) + h_2^2 \cos(2\phi)] \sin^2(\theta) \right\} \right\} \\ 4 \frac{a^5}{r^5} \left\{ g_3^0 \cos(\theta) \left( 1 - \frac{5}{2} \sin^2(\theta) \right) + \sqrt{\frac{3}{2}} [g_3^1 \cos(\phi) + h_3^1 \sin(\phi)] \right. \\ \left. \times \sin(\theta) \left( 2 - \frac{5}{2} \sin^2(\theta) \right) \right. \\ \left. + \sqrt{\frac{15}{4}} [g_3^2 \cos(2\phi) + h_3^2 \sin(2\phi)] \cos(\theta) \sin^2(\theta) \right. \\ \left. + \sqrt{\frac{5}{8}} [g_3^3 \cos(3\phi) + h_3^3 \sin(3\phi)] \sin^3(\theta) \right\} \\ -\frac{a^5}{r^5} \left\{ \frac{3}{2} g_3^0 \sin(\theta) \left( 1 - 5 \cos^2(\theta) \right) + \sqrt{\frac{3}{2}} [g_3^1 \cos(\phi) + h_3^1 \sin(\phi)] \right. \\ \left. \times \cos(\theta) \left( 2 - \frac{15}{2} \sin^2(\theta) \right) \right. \\ \left. + \sqrt{\frac{15}{4}} [g_3^2 \cos(2\phi) + h_3^2 \sin(2\phi)] \sin(\theta) (2 - 3 \sin^2(\theta)) \right. \\ \left. + \sqrt{\frac{45}{8}} [g_3^3 \cos(3\phi) + h_3^3 \sin(3\phi)] \sin^2(\theta) \cos(\theta) \right\} \\ -\frac{a^5}{r^5} \frac{1}{\sin(\theta)} \left\{ \sqrt{\frac{3}{2}} [-g_3^1 \sin(\phi) + h_3^1 \cos(\phi)] \sin(\theta) \left( 2 - \frac{5}{2} \sin^2(\theta) \right) \right. \\ \left. + \sqrt{15} [-g_3^2 \sin(2\phi) + h_3^2 \cos(2\phi)] \cos(\theta) \sin^2(\theta) \right. \\ \left. + \sqrt{\frac{45}{8}} [-g_3^3 \sin(3\phi) + h_3^3 \cos(3\phi)] \sin^3(\theta) \right\} \end{bmatrix} +$$

## References

- [1] D. Honess, O. Quinlan, Astro Pi: Running your code aboard the International Space Station, *Acta Astronaut.* 138 (2017) 43–52, <http://dx.doi.org/10.1016/j.actaastro.2017.05.023>.
- [2] S.P. Savin, O. Balan, N. Borodkova, E. Budnik, N. Nikolaeva, V. Prokhorenko, T. Pulkkinen, N. Rybjeva, J. Safrankova, I. Sandahl, E. Amata, U. Auster, G. Bellucci, A. Blagau, J. Blecki, J. Buechner, M. Ciobanu, E. Dubinin, Y. Yermolaev, M. Echim, A. Fedorov, V. Formisano, R. Grard, V. Ivchenko, F. Jiricek, J. Juchniewicz, S. Klimov, V. Korepanov, H. Koskinen, K. Kudela, R. Lundin, V. Lutsenko, O. Marghitu, Z. Nemecek, B. Nikutowski, M. Nozdrachev, S. Orsini, M. Parrot, A. Petrukovich, N. Pissarenko, S. Romanov, J. Rauch, J. Rustenbach, J.A. Sauvaud, E.T. Sarris, A. Skalsky, J. Smilauer, P. Triska, J.G. Trotignon, J. Vojta, G. Zastenker, L. Zelenyi, Y. Agafonov, V. Grushin, V. Khrapchenkov, L. Prech, O. Santolík, Interball magnetotail boundary case studies, *Adv. Space Res.* 20 (4–5) (1997) 999–1015, [http://dx.doi.org/10.1016/S0273-1177\(97\)00508-5](http://dx.doi.org/10.1016/S0273-1177(97)00508-5).
- [3] I. Dandouras, A. Barthe, E. Penou, S. Brunato, H. Rème, L.M. Kistler, M.B. Bavassano-Cattaneo, A. Blagau, Cluster Ion Spectrometry (CIS) data in the Cluster Active Archive (CAA), in: *The Cluster Active Archive, in: Astrophysics and Space Science Proceedings*, Vol. 11, 2010, pp. 51–72, [http://dx.doi.org/10.1007/978-90-481-3499-1\\_3](http://dx.doi.org/10.1007/978-90-481-3499-1_3).
- [4] A. Blagau, I. Dandouras, A. Barthe, S. Brunato, G. Facskó, V. Constantinescu, In-flight calibration of the Hot Ion Analyser on board Cluster, *Geosci. Instrum. Methods Data Syst.* 3 (1) (2014) 49–58, <http://dx.doi.org/10.5194/gi-3-49-2014>.
- [5] F. Plaschke, H.-U. Auster, D. Fischer, K.-H. Fornaçon, W. Magnes, I. Richter, D. Constantinescu, Y. Narita, Advanced calibration of magnetometers on spin-stabilized spacecraft based on parameter decoupling, *Geosci. Instrum. Methods Data Syst.* 8 (1) (2019) 63–76, <http://dx.doi.org/10.5194/gi-8-63-2019>.
- [6] Phidgets, 2021, <https://www.phidgets.com/?tier=3&catid=10&pcid=8&prodid=1038> [Accessed: Oct. 2021].
- [7] STMicroelectronics, 2021, <https://www.st.com/en/mems-and-sensors/lsm9ds1.html> [Accessed: Oct. 2021].
- [8] Team Narwhals Report, 2021, [https://github.com/NarwhalsTeam/Narwhals\\_Astro\\_Pi/blob/main/Narwhals\\_report\\_eng.pdf](https://github.com/NarwhalsTeam/Narwhals_Astro_Pi/blob/main/Narwhals_report_eng.pdf) [Accessed: Oct. 2021].
- [9] J.D. Jackson, *Classical Electrodynamics*, third ed., 1998.
- [10] Team Mag-AZ Report, 2021, <https://github.com/LouXonline/Mag-AZ> [Accessed: Oct. 2021].
- [11] Celestrak site, 2021, <https://celestrak.com> [Accessed: Oct. 2021].
- [12] B. Rhodes, Skyfield: High precision research-grade positions for planets and Earth satellites generator, 2019, [arXiv:1907.024](https://arxiv.org/abs/1907.024).
- [13] Skyfield package, 2021, <https://rhodesmill.org/skyfield/> [Accessed: Oct. 2021].
- [14] C.C. Finlay, C. Kloss, N. Olsen, M.D. Hammer, L. Tøffner-Clausen, A. Grayver, A. Kuvshinov, The CHAOS-7 geomagnetic field model and observed changes in the South Atlantic Anomaly, *Earth Planets Space* 72 (1) (2020) 156, <http://dx.doi.org/10.1186/s40623-020-01252-9>, [arXiv:2010.11313](https://arxiv.org/abs/2010.11313).
- [15] CHAOS Package, 2021, <http://www.spacecenter.dk/files/magnetic-models/CHAOS-7/> [Accessed: Oct. 2021].
- [16] NASA, International Space Station Facts and Figures, 2021, <https://www.nasa.gov/feature/facts-and-figures> [Accessed: Oct. 2021].
- [17] P. Alken, E. Thébaud, C.D. Beggan, H. Amit, J. Aubert, J. Baerenzung, T.N. Bondar, W.J. Brown, S. Califf, A. Chambodut, A. Chulliat, G.A. Cox, C.C. Finlay, A. Fournier, N. Gillet, A. Grayver, M.D. Hammer, M. Holschneider, L. Huder, G. Hulot, T. Jager, C. Kloss, M. Korte, W. Kuang, A. Kuvshinov, B. Langlais, J.M. Léger, V. Lesur, P.W. Livermore, F.J. Lowes, S. Macmillan, W. Magnes, M. Mandea, S. Marsal, J. Matzka, M.C. Metman, T. Minami, A. Morschhauser, J.E. Mound, M. Nair, S. Nakano, N. Olsen, F.J. Pavón-Carrasco, V.G. Petrov, G. Ropp, M. Rother, T.J. Sabaka, S. Sanchez, D. Saturnino, N.R. Schnepf, X. Shen, C. Stolle, A. Tangborn, L. Tøffner-Clausen, H. Toh, J.M. Torta, J. Varner, F. Vervelidou, P. Vigneron, I. Wardinski, J. Wicht, A. Woods, Y. Yang, Z. Zeren, B. Zhou, International Geomagnetic Reference Field: the thirteenth generation, *Earth Planets Space* 73 (1) (2021) 49, <http://dx.doi.org/10.1186/s40623-020-01288-x>.
- [18] N. Barros e Sá, L. Faria, B. Alves, M. Cymbron, Modelling the Earth's magnetic field with magnetometer data from a Raspberry Pi on board the ISS, 2021, [arXiv:2108.00123](https://arxiv.org/abs/2108.00123).
- [19] D.E. Winch, D.J. Ivers, J.P.R. Turner, R.J. Stening, Geomagnetism and Schmidt quasi-normalization, *Geophys. J. Int.* 160 (2) (2005) 487–504, <http://dx.doi.org/10.1111/j.1365-246X.2004.02472.x>.
- [20] K. Lundal, Pure Python International Geomagnetic Reference Field, 2022, <http://dx.doi.org/10.5281/zenodo.5962661>.
- [21] W. Magnes, O. Hillenmaier, H.U. Auster, P. Brown, S. Kraft, J. Seon, M. Delva, A. Valavanoglou, S. Leitner, D. Fischer, G. Berghofer, Y. Narita, F. Plaschke, M. Volwerk, J. Wilfinger, C. Strauch, J. Ludwig, D. Constantinescu, K.H. Fornaçon, K. Gebauer, D. Hercik, I. Richter, J.P. Eastwood, J.P. Luntama, A. Hilgers, M. Heil, G.W. Na, C.H. Lee, Space weather magnetometer aboard GEO-KOMPSAT-2A, *Space Sci. Rev.* 216 (8) (2020).
- [22] D.O. Constantinescu, H.-U. Auster, M. Delva, O. Hillenmaier, W. Magnes, F. Plaschke, Maximum-variance gradiometer technique for removal of spacecraft-generated disturbances from magnetic field data, *Geosci. Instrum. Methods Data Syst.* 9 (2) (2020) 451–469, <http://dx.doi.org/10.5194/gi-9-451-2020>.
- [23] E. Doornbos, L. Massarweh, A. Menicucci, E. Iorfida, C. Stolle, M. Rother, G. Kervalishvili, J. Rauber, Feasibility of Using Platform Magnetometers to Observe and Detect Space Weather Events, *Tech. Rep.*, European Space Agency, 2018.
- [24] B.J. Anderson, K. Takahashi, B.A. Toth, Sensing global Birkeland currents with iridium® engineering magnetometer data, *Geophys. Res. Lett.* 27 (24) (2000) 4045–4048, <http://dx.doi.org/10.1029/2000GL000094>.
- [25] P. Alken, N. Olsen, C.C. Finlay, Co-estimation of geomagnetic field and in-orbit fluxgate magnetometer calibration parameters, *Earth Planets Space* 72 (1) (2020) 49, <http://dx.doi.org/10.1186/s40623-020-01163-9>.
- [26] N. Olsen, G. Albin, J. Bouffard, T. Parrinello, N. Tøffner-Clausen, Magnetic observations from CryoSat-2: calibration and processing of satellite platform magnetometer data, *Earth Planets Space* 72 (1) (2020) 48, <http://dx.doi.org/10.1186/s40623-020-01171-9>.
- [27] N. Olsen, Magnetometer data from the GRACE satellite duo, *Earth Planets Space* 73 (1) (2021) 62, <http://dx.doi.org/10.1186/s40623-021-01373-9>.
- [28] P. Alken, N. Olsen, C.C. Finlay, Co-estimation of geomagnetic field and in-orbit fluxgate magnetometer calibration parameters, *Earth Planets Space* 72 (1) (2020) 49, <http://dx.doi.org/10.1186/s40623-020-01163-9>.
- [29] A. Kuvshinov, A. Grayver, L. Tøffner-Clausen, N. Olsen, Probing 3-D electrical conductivity of the mantle using 6 years of Swarm, CryoSat-2 and observatory magnetic data and exploiting matrix Q-responses approach, *Earth Planets Space* 73 (1) (2021) 67, <http://dx.doi.org/10.1186/s40623-020-01341-9>.